



# Simplified modeling of the impact of lithospheric-scale geological processes on thermal histories and low-temperature thermochronometers

Dawn A. Kellett<sup>1,\*</sup> and David M. Whipp<sup>2,\*</sup>

Correspondence: Dawn A. Kellett (dawn.kellett@nrcan-rncan.gc.ca)

Abstract. Many geological processes influence or perturb the thermal state of the lithosphere. This presents a challenge for relating thermal history data modeled from thermochronometers such as apatite and zircon fission-track and (U-Th)/He dating to geological evolution, a primary goal of many thermochronology studies. Here we address this challenge by exploring the thermal and thermochronological evolution of tracked rock parcels in 1D models that simulate key lithospheric geological processes, including erosional exhumation, sedimentary burial and exhumation, dip-slip faulting and delamination of the lithospheric mantle. We compare results from common depth history scenarios in which the Moho either experiences exhumation/burial or remains at a fixed depth balanced by crustal flux and erosion. Results show that Moho depth changes have a significant effect on thermal histories and thermochronometers, though this is not often considered in thermal history studies. Further, our results show that the recorded response of thermal histories/thermochronometers in the upper crust and geological processes that disrupt the crustal thermal field may be disassociated in time, because of the time and length scales of different heat transfer mechanisms. For example, a delamination event produces younger thermochronometer ages than an identical crustal exhumation history without delamination, but younger ages do not record the timing of delamination.

#### 1 Introduction

Heat in the Earth's lithosphere is a complex process variable, and many geological processes influence or perturb the lithospheric geothermal gradient. The thermal evolution of the lithosphere is typically studied from surface samples that may have not only experienced a dynamic geothermal gradient but also changed position relative to the Earth's surface through geological time. Consequently, the relationship between the geological processes a rock has experienced on its path to the present and that rock's thermal history is of broad interest to the geological community.

Low-temperature thermochronology is a field of research in which the thermally controlled retention of radioactive decay products in geological materials is measured to reconstruct mineral and rock thermal histories, especially regarding their passage through the upper crust ( $< 350^{\circ}$  C). Such thermal histories are most often constructed by inverting low-temperature

<sup>&</sup>lt;sup>1</sup>Geological Survey of Canada-Atlantic, Natural Resources Canada, Dartmouth, B2Y 4A2, Canada

<sup>&</sup>lt;sup>2</sup>Department of Geosciences and Geography, University of Helsinki, 00014 University of Helsinki, Helsinki, Finland

<sup>\*</sup>These authors contributed equally to this work.





thermochronological data using software to identify envelopes of most likely thermal histories, such as HeFTy (Ketcham, 2005) or QTQt (Gallagher, 2012).

While such inversions of rock thermochronometer data are highly informative depictions of rock thermal histories, the ultimate goal of most low-temperature thermochronological studies is to relate thermal histories to geological processes, in order to reconstruct the tectonic and/or landscape evolution of the upper crust. This requires an ability to model the dynamic evolution of the lithospheric thermal field (e.g., Ehlers, 2005). Software for inverting thermal histories, such as HeFTy or QTQt, is user friendly, widely used, and sophisticated in its ability to address complex retention behaviors of the various low-temperature thermochronometers. Yet, the ability to relate those thermal histories to geological processes, described for example in Flowers et al. (2015) as stepping from "level 2 – thermal model outputs" to "level 3 – geological interpretation", remains a critical interpretive challenge.

There are a range of existing 2D and 3D surface process, kinematic and/or geodynamic modeling software packages available that solve the heat equation through time in response to geological processes such as faulting, fluvial erosion, or viscous crustal flow that can, or could be adapted to, forward model or invert thermochronometer age data, such as Pecbue (Braun, 2003) or Badlands and Underworld (Salles and Hardiman, 2016; Mansour et al., 2020). However, these approaches are computationally expensive and require steep learning curves, presenting barriers to those in pursuit of simple parameter exploration.

In this contribution, we explore first-order relationships between the thermal evolution of the lithosphere and the thermochronological record using a new 1D modeling code with thermokinematic capabilities that bridges between the existing thermal history modeling tools and more complex 2D and 3D thermokinematic modeling software. The simplified relationships that we explore between rock thermochronometer ages, low-temperature thermal histories, and geological processes are aimed at improving our ability to make these relationships in more complex empirical studies. We consider an example set of 1D scenarios involving erosion, sedimentary burial, thrust and extensional faulting, and delamination of the lithospheric mantle. In these models, we examine the conditions under which thermal histories deviate from or track with depth histories, and how the resulting thermochronometer ages and time lags between thermochronometers relate to the geological process(es) triggering rock heating/cooling.

## 2 Methods

45

# 2.1 T<sub>c</sub>1D: 1D heat transfer and thermochronometer age prediction model

T<sub>c</sub>1D, the modeling software used in this study, is a 1D thermal and thermochronometer age prediction software package written in Python that simulates the dynamic thermal effects of common geological processes at the scale of the full lithosphere (Whipp, 2022). The software uses recorded thermal histories to calculate various thermochronometer ages for particles that reach the model surface during and at the end of simulations. The design of T<sub>c</sub>1D is deliberately simple, allowing the user to vary a range of parameters and quickly explore their effects in (multi-)thermochronometry datasets. Thus, the goal is not to simulate all the geological details of a complex geodynamic process like lithospheric delamination or post-orogenic collapse, but rather to produce first-order dynamic "geological" heat transfer models and explore the relationships between





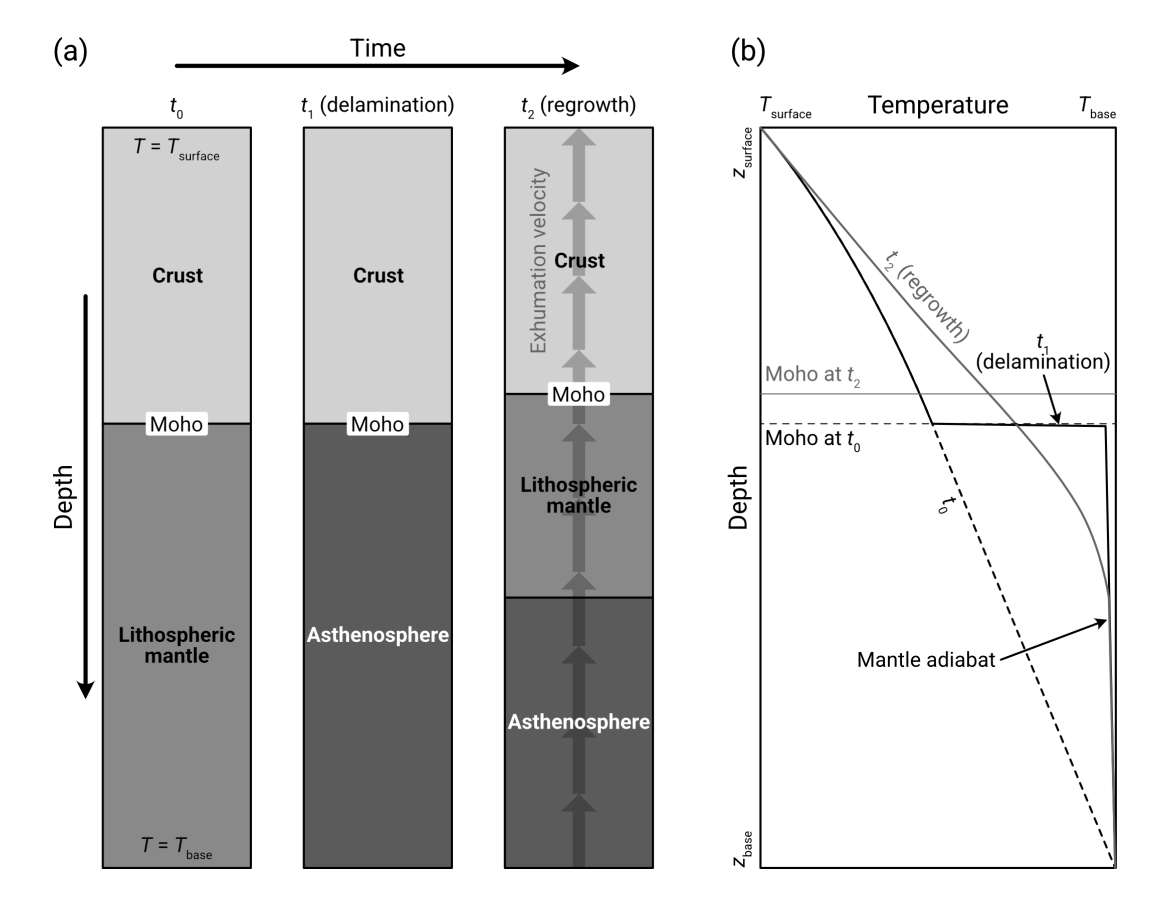


Figure 1. Schematic overview of the time evolution of an example  $T_c1D$  model of lithospheric delamination and the corresponding geotherms. (a) Three lithospheric-scale columns representing the initial thermal solution ( $t_0$ , left), moment of instantaneous lithospheric delamination ( $t_1$ , center), and dynamic regrowth of mantle lithosphere millions of years after delamination ( $t_2$ , right). The thermal boundary conditions are constant through time (left), and erosional exhumation advects heat and the Moho toward the surface after delamination (right). (b) Geotherms for each of the three model stages showing the thermal effects of delamination and thermal advection.

those models, the corresponding depth and thermal histories experienced by particles reaching the model surface, and calculated low-temperature thermochronometry ages and characteristics (Fig. 1). Thermochronometer systems supported in T<sub>c</sub>1D include apatite (U-Th)/He (AHe), apatite fission-track (AFT), zircon (U-Th)/He (ZHe), and zircon fission track (ZFT).

 $T_c 1D$  uses the finite-difference method to solve the transient heat transfer equation in 1D in the crust and lithospheric mantle, including the thermal effects of advection and volumetric heat production. Temperatures are fixed at the surface and base of the model, and the initial thermal field is calculated at a steady state using an optional advection velocity specified for the start of the simulation. The temperature calculation forward in time from the initial state can use either an implicit or explicit finite-difference solution with user-defined time steps. Rock thermal and physical properties are defined separately for the crust, lithospheric mantle, and asthenosphere. A variety of erosion models are built into  $T_c 1D$  allowing users to explore many different burial (i.e., negative erosion) and exhumation histories (Whipp, 2022).





Thermal histories are recorded by tracking the temperature of particles that reach the model surface at the end of the simulation, and optionally at specified intervals during the simulation. The thermal histories are used to predict thermochronometer ages using the radiation damage accumulation and annealing models for AHe (Flowers et al., 2009) and ZHe (Guenthner et al., 2013), and the fission track annealing models for AFT (Ketcham et al., 1999) and ZFT (van der Beek et al., 1995) using the kinetics of Tagami et al. (1998) or Rahn et al. (2004). The program used for AHe and ZHe age predictions is from Ketcham et al. (2018), the AFT age prediction program is from Ketcham et al. (2000) as implemented in Braun et al. (2012), and the ZFT age prediction code was ported to Python following its implementation in Braun et al. (2012).

### 2.2 Modeled scenarios

Five common geological processes are explored with  $T_c1D$ . The first set of 12 models explores various styles of erosional exhumation (EE), followed by 6 sedimentary burial models (SB), 4 thrust faulting (TF) models, 4 extensional faulting (EF) models, and 4 lithospheric delamination models (DL) (Table 1, Fig. 2). The different geological scenarios primarily affect movement of material within the model, resulting in heat transfer by advection and displacement of a thermal history tracking particle. Each model has a thickness of 125 km and a final Moho depth of 35 km. More detailed descriptions of each scenario are given below and other common model parameters are summarized in Table 2.

## 2.2.1 Erosional exhumation (EE) models

The EE models explore the effect of a time-varying rate of erosional exhumation on predicted thermochronometer ages over a 50 Myr duration. In these models, the rate of erosional exhumation is either constant, has a step-function increase after 5 or 45 Myr, or decreases following an exponential function with different characteristic times for decay. The total amount of exhumation is either 10 or 20 km, and the constant-rate models produce this amount of exhumation linearly over 50 Myr. The step-function models have either 5 or 10 km of exhumation over the initial or final 5 Myr of the simulation, with the remaining 5 or 10 km of exhumation evenly distributed over the remainder of the simulation time. The exponential models produce 10 km of exhumation with characteristic decay times of 2, 10 or 50 Myr, as well as 20 km of exhumation with a characteristic decay time of 2 Myr. The internal radiogenic heat production in the crust is either average (1 μW·m<sup>-3</sup>) or high (2 μW·m<sup>-3</sup>) (Table 1; Fig. 2).

For each exhumation style, the EE models also consider two variations: one where the Moho depth shallows during exhumation and another where the Moho depth remains constant. The models for which the Moho shallows during exhumation (hereafter referred to as MM, for moving Moho, see Fig. 2b) simulate erosional exhumation in a post-tectonic setting where the crust is thinned due to erosion driven by isostasy (e.g., type 3 of Wolf et al., 2022), which results in movement of the entire lithosphere toward the surface. Thus, these models have a velocity field that is constant across the entire model thickness. In contrast, models with a constant Moho depth (hereafter referred to as FM, for fixed Moho, see Fig. 2a) represent a steady-state, syn-collisional setting in which erosional exhumation is balanced by a crustal mass flux via shortening and/or crustal flow at depth (e.g., type 2 of Wolf et al., 2022). In this case, the erosional exhumation velocity is only applied to the model crust. In both cases, the Moho depth at the end of the simulation is 35 km. It is illustrative to compare both scenarios (FM and MM) because





Table 1. T<sub>c</sub>1D modelled scenarios

Model	IHP		Time intervals (Ma in the model framework)										
		55 - 50	50 - 45	45 - 40	40 - 35	35 - 30	30 - 25	25 - 20	20 - 15	15 - 10	10 - 5	5 – 0	
EE1	High	_				Е	rode 10 km,	constant rate					
EE2	Avg	-	Erode 10 km, constant rate										
EE3	Avg	-	CE 5 km Erode 5 km, constant rate										
EE4	Avg	-	Erode 5 km, constant rate CE 5 km										
EE5	High	_	Erode 20 km, constant rate										
EE6	Avg	1	Erode 20 km, constant rate										
EE7	Avg	_	CE 10 km	Erode 10 km, constant rate									
EE8	Avg	-		Erode 10 km, constant rate CE 10 km									
EE9	High	ı	Erode 10 km, exponentially decaying erosion with short decay constant										
EE10	Avg	ı	Erode 10 km, exponentially decaying erosion with medium decay constant										
EE11	Avg	-	Erode 10 km, exponentially decaying erosion with long decay constant										
EE12	Avg	-	Erode 20 km, exponentially decaying erosion with short decay constant										
SB1	High	_	Deposit 9 km Erode 10 km, constant rate										
SB2	Avg	1	Deposit 9 km Erode 10 km, constant rate										
SB3	High	-	Deposit 9 km				Erode 10 km, constant rate						
SB4	Avg	-	Deposit 9 km				Erode 10 km, constant rate						
SB5	High	-	D9 Erode 10 km over 49 Myr, constant rate										
SB6	Avg	ı	D9 Erode 10 km over 49 Myr, constant rate										
TF1	Avg	SS	SS 6.25 km Erode 8.75 km, constant rate (0.5 km above fault in HW)										
			FW uplift										
TF2	Avg	SS	6.25 km	Erode 8.75 km, constant rate (0.5 km below fault in FW)									
			HW burial										
TF3	Avg	SS	12.5 km	Erode 2.5 km, constant rate (0.5 km above fault in HW)									
			FW uplift										
TF4	Avg	SS	0.0 km	Erode 2.5 km, constant rate (0.5 km below fault in FW)									
			HW burial										
EF1	Avg	SS	6.25 km	Erode 8.75 km, constant rate (0.5 km below fault in FW)									
			HW uplift										
EF2	Avg	SS	6.25 km	Erode 8.75 km, constant rate (0.5 km above fault in HW)									
			FW burial										
EF3	Avg	SS	12.5 km	Erode 2.5 km, constant rate (0.5 km below fault in FW)									
			HW uplift										
EF4	Avg	SS	0.0 km	Erode 2.5 km, constant rate (0.5 km above fault in HW)									
			FW burial										
DL1	Avg	SS	DL 15 km*	Erode 15 km, constant rate									
DL2	Avg	SS	DL 15 km*	7 1 3 3 2									
DL3	Avg	SS	DL 15 km*	Erode 15 km, exponentially decaying erosion with medium decay constant									
DL4	Avg	SS	DL 15 km*	* Erode 15 km, exponentially decaying erosion with long decay constant									

Scenarios have a 50 (EE and SB) or 55 (TF, EF, DL) Myr duration. TF, EF, and DL models include an initial 5 Myr of thermal steady state (SS, 55-50 Ma) before faulting/delamination. Acronyms and table symbols: IHP, internal heat production; EE, erosional exhumation; SB, sedimentary burial; TF, thrust faulting; EF, extensional faulting; DL, delamination of the continental lithospheric mantle; D9, deposit 9 km in 1 Myr; CE, constant erosion rate; \*, delamination of the subcontinental lithospheric mantle and juxtaposition of asthenosphere against the base of the crust is performed instantaneously in the model at t=50 Ma; High IHP, 2  $\mu$ W·m<sup>-3</sup>; Avg IHP, 1  $\mu$ W·m<sup>-3</sup>.





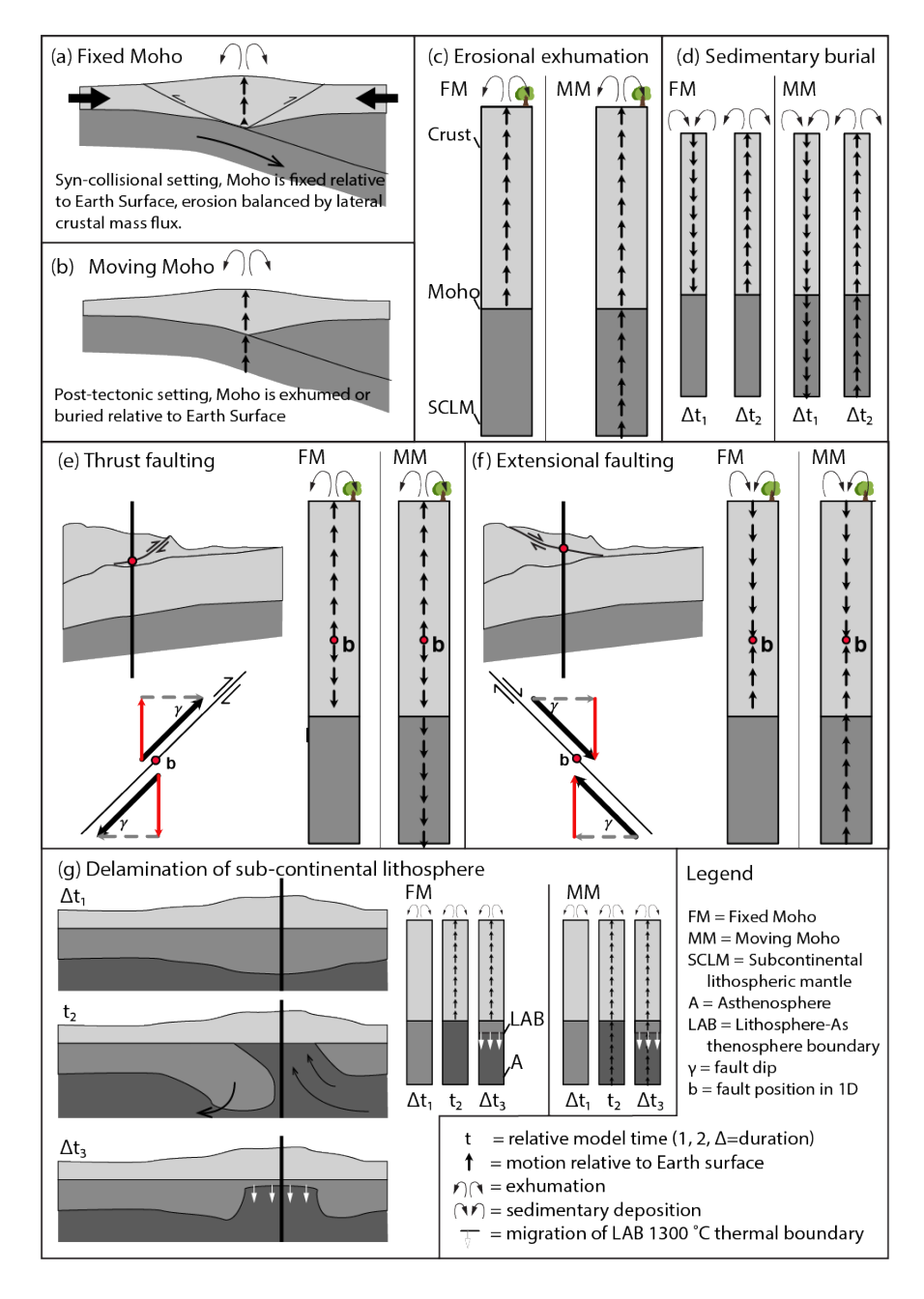


**Figure 2.** Schematic diagrams of 1D model types listed in Table 1, with the vertical black line depicted in all cross sections simulating the 1D position of the model. Each scenario is modeled with both a fixed (a) and moving (b) Moho, broadly analogous to syn- and post-tectonic settings. Modeled scenarios include explorations of (c) erosional exhumation, (d) sedimentary burial, (e) thrust faulting, (f) extensional faulting and (g) delamination of the sub-continental lithospheric mantle.





**Table 2.** T<sub>c</sub>1D model parameters

Parameter	Value*	Unit							
General parameters									
Thickness	125	km							
Spatial resolution	0.5	km							
Duration	50 - 55	Myr							
Time step, explicit	500	yr							
Time step, implicit	5000	yr							
Initial Moho depth	35 - 50	km							
Thermal parameters									
Surface temperature	0	°C							
Basal temperature	1300	°C							
Density <sup>†</sup>	2850, 3250, 3250	$kg \cdot m^{-3}$							
Heat capacity <sup>†</sup>	800, 1000, 1000	$J{\cdot}kg^{-1}K^{-1}$							
Thermal conductivity <sup>†</sup>	2.75, 2.5, 20.0	$W{\cdot}m^{-1}K^{-1}$							
Volumetric heat prod. <sup>†</sup>	1–2, 0, 0	$\mu \text{W} \cdot \text{m}^{-3}$							
Thermochronometer parameters									
Grain radius <sup>‡</sup>	45, 60	$\mu$ m							
U concentration <sup>‡</sup>	10, 100	ppm							
Th concentration <sup>‡</sup>	40, 40	ppm							

<sup>\*</sup> Varied parameters shown as ranges

the evolution of the Moho depth is not often considered when modeling low-T thermochronological data, and yet it exerts an influence on the thermal structure of the crust, and hence on thermochronometer ages. We have chosen to present scenarios in which the final Moho depth is identical between the two runs, rather than having equal starting Moho depths, because it is more representative of the challenge facing the geologist–a myriad of different possible trajectories through temperature-depth-time (T-d-t) space could produce the present day thermal and geological structure of the crust and pattern of thermochronological data.

## 2.2.2 Sedimentary burial (SB) models

100

The SB models are somewhat similar to the EE models but involve a phase of sedimentary deposition at the start of the model prior to erosional exhumation. In each case, 9 km of sediment is initially deposited over 1, 10, or 20 Myr resulting in variable sedimentation rates referred to as low, intermediate and high. Following deposition, 10 km of material is eroded (9 km of sediment and 1 km of basement) over the remainder of the 50 Myr model duration. In contrast to the EE models, however,

 $<sup>^\</sup>dagger$  List order: Crust, mantle lithosphere, as thenosphere

<sup>&</sup>lt;sup>‡</sup> List order: Apatite, zircon



120

125

130



only moving Moho cases are considered and thus the sedimentation and erosion velocities are applied across the full model thickness. In addition, model variants include average  $(1 \ \mu W \cdot m^{-3})$  and high  $(2 \ \mu W \cdot m^{-3})$  crustal radiogenic heat production, similar to the EE models (Table 1; Fig. 2).

# 2.2.3 Thrust faulting (TF) models

The TF models are designed to simulate the contrasting exhumation histories experienced by rocks in the hanging wall and footwall of thrust faults. Crustal-scale faults commonly show contrasting thermochronometer age patterns between hanging wall (HW) and footwall (FW) samples, particularly for thrust and normal dip-slip fault types in which rocks from different structural levels may be juxtaposed (e.g., Stockli, 2005). Classical 1D thermal models of thrust faulting, first presented by Oxburgh and Turcotte (1974), have typically simulated the thermal effects of thrust activity via instantaneous stacking of the crustal thrust nappes. This creates an initial sharp step in temperature-depth space that duplicates the geothermal gradient in the upper crust, subsequent thermal relaxation in which the HW is cooled and the FW is heated by their juxtaposition across the fault, and an eventual re-establishment of the conductive geothermal gradient across the thickened crust. Associated crustal thickening would likely promote erosional exhumation due to isostatic uplift, particularly focused in the HW. More complex 2D thrust fault and fold-and-thrust belt models have compared low temperature thermochronology data against forward modeled fold-and-thrust belt evolutions involving one or multiple active structures, predicting along-strike patterns in thermal history and thermochronometer ages between the footwall and hanging wall (e.g., U-shaped patterns; Lock and Willett, 2008), and across fold belts (e.g., McQuarrie and Ehlers, 2015; McQuarrie et al., 2017).

The TF models target a model design of intermediate complexity, using a single fault system that can be activated for a desired duration, specified slip rate, and fault dip angle, and simultaneous with surface erosion (or deposition if subsidence occurs). Faulting scenarios are explored in  $T_c 1D$  using a framework in which the fault is initially positioned at a specified depth b, with a prescribed dip angle  $\gamma$ , and a slip rate of v (Fig. 2e). Movement across the fault is divided between the HW and FW via a partitioning factor  $\lambda$ , such that  $\lambda=1$  represents a fixed HW and  $\lambda=0$  represents a fixed FW. The corresponding vertical (1D) components of velocity due to fault slip in the footwall,  $v_{z,\text{fw}}$ , and hanging wall,  $v_{z,\text{hw}}$ , are:

$$v_{z,\text{fw}} = \lambda v \sin \gamma$$
 (1)

$$v_{z,\text{hw}} = -(1 - \lambda)v\sin\gamma\tag{2}$$

In TF scenarios, the FW is advected downwards and the HW is advected upwards during faulting (Fig. 2e). Frictional heating along the fault surface is ignored. As the horizontal component of motion and heat transfer is also ignored, the exercise of comparing contrasting thermal histories in selected HW and FW positions effectively requires two different 1D starting columns that converge when the total desired fault slip is completed (see Fig. A1). In such cases, the tracking particles in the HW and FW of two different models reach the same depth at the end of faulting and are subsequently exhumed by the same amount to the surface over the model duration. The TF models begin with a 5 Myr period with no fault movement or exhumation followed by a 5 Myr period of fault activity on a fault with a slip rate of v = 5 km/Myr and dip angle of  $\gamma = 30^{\circ}$ . Partitioning factors of  $\lambda = 0.5$  and  $\lambda = 0$  are used, with initial fault depths of b = 15.5 and 2 km for tracking particles located



160

165

170



500 m above and below the fault in the HW and FW, respectively. The difference in initial fault depth relates to how fault motion is defined. Final surface particles in the hanging wall will move upwards during fault motion, while particles in the footwall will move downwards. In both cases, the reference frame maintains a constant distance above or below the fault, resulting in the fault following the movement of the tracking particle (Fig. A1). The final stage is erosional exhumation of the tracking particle to the surface over the remaining 45 Myr of the simulation. Thus, all TF models have a duration of 55 Myr, over which 15 km of exhumation occurs. Both FM and MM kinematics are used, but only the average crustal radiogenic heat production value is considered (1  $\mu$ W·m<sup>-3</sup>) (Table 1; Fig. 2).

### 2.2.4 Extensional fault (EF) models

The EF models are effectively identical to the TF models described above, with the only significant difference being a reversed fault slip direction. The models feature a 5 Myr period of no motion, 5 Myr of faulting, and 45 Myr of erosional exhumation following faulting, totaling 15 km of exhumation over the 55 Myr model duration. Similar to the TF models, fault motion advects model particles in the HW and FW of paired models to the same depths before equal amounts of exhumation transport them to the surface. As before, particles located 500 m above and below the fault are tracked, which requires initial fault depths
of b = 14.5 and 3 km for tracking particles in the FW and HW, respectively. FM and MM scenarios are considered and an average crustal radiogenic heat production (1 μW·m<sup>-3</sup>) is used.

# 2.2.5 Lithospheric delamination (DL) models

The DL models simulate the thermal and thermochronometer age effects of instantaneous removal of the mantle lithosphere, its replacement by asthenospheric material, and thermal relaxation during subsequent erosional exhumation. Lithospheric delamination and dripping are density-driven processes in which the sub-continental lithospheric mantle (and possibly lower crust) founders, detaches, and sinks into the asthenosphere, juxtaposing hot asthenosphere against the base of the remaining crust (Ducea, 2011; Göğüş and Ueda, 2018; McMillan and Schoenbohm, 2023). Signatures of past delamination and drip are thought to include a shift in magmatism towards more deeply-sourced, mafic magmatism (Kay and Mahlburg Kay, 1993; Drew et al., 2009) and rapid surface uplift during the foundering or detachment stages (Garzione et al., 2006, 2008), sometimes preceded by burial/deposition and heating during the foundering stage (McMillan and Schoenbohm, 2023). For more recent lithospheric removal events, the lithospheric mantle may be imaged as thin or non-existent (e.g., Bezada et al., 2014). In some cases, the delaminated slab may still be imageable in the mantle (e.g., Zandt et al., 2004; Bao et al., 2014; Bezada et al., 2014).

Because delamination produces both a thermal and surface process response due to uplift or subsidence/deposition, its impact on the upper crust may be recorded in the low-temperature thermochronology record. Hence the timing and nature of lithospheric delamination have been studied using low-temperature thermochronometry, and/or interpreted inflections in exhumation rate based upon low-temperature thermochronometer data have been linked to lithospheric delamination as a causative process (e.g., Dai et al., 2013; Bao et al., 2014; Bidgoli et al., 2015; Fraser et al., 2021).

The DL models simulate removal of the continental lithospheric mantle and juxtaposition of the asthenosphere against the base of the crust, followed by exhumation over the remainder of the model duration. Since delamination and drip involve both





top-down surface processes and bottom-up heat conduction/advection, it is useful to examine the timescales and interactions of these erosional and heat-transfer processes. The DL models feature 5 Myr at the start with no exhumation or delamination, instantaneous delamination of the entire mantle lithosphere after 5 Myr, and 15 km of erosional exhumation over the remaining 50 Myr of the model time. Temperatures in the asthenospheric material are defined by a mantle adiabatic temperature gradient (Turcotte and Schubert, 2014) initially for the entire mantle at 5 Myr and the mantle lithosphere regrows by conductive cooling (Fig. 2). Because we have not attempted to link a surface process model to the 1D models in T<sub>c</sub>1D, we explore delamination under various exhumation scenarios, including a constant rate of erosional exhumation following delaminationand exhumation with an exponential function with varying characteristic decay times of 2, 10, and 50 Myr. Both FM and MM scenarios are considered with an initial Moho depth of 50 km for the MM scenarios, such that the Moho ends up at 35 km depth for both models. Only an average crustal radiogenic heat production value is considered (1 μW·m<sup>-3</sup>).

## 185 2.3 Additional model design considerations

Note that all models involve a significant amount of erosional exhumation because the calculated thermochronometer ages and closure temperatures in the models rely on the tracking particle reaching the surface at the end of the model run (hereafter called the final surface particle). Any scenarios involving insufficient exhumation will not capture the thermal history of the geological process under investigation (i.e., it will yield an unreset age roughly equivalent to the duration of the model). In this way,  $T_c 1D$  can also be employed to explore minimum erosion magnitudes required to "capture" information about past geological processes using low-temperature thermochronology.

In addition, the complex effects of alpha damage accumulation on He retention in apatite and especially in zircon renders it impossible to accurately simulate He diffusion behavior in any models in which the final surface particle begins the simulation in a position of He and alpha damage accumulation (see also Whipp et al., 2022). Crystal damage is thought to anneal in a similar way, and under similar temperature conditions to fission tracks (Flowers et al., 2009; Guenthner et al., 2013; Guenthner, 2021). Hence, most of the scenarios explored below involve a starting depth for which open system behavior is expected, and zircon or apatite should not have accumulated any alpha damage ( $\sim 300^{\circ}$  C). Where this is not the case, the implications are discussed. This is a recommended practice when using the  $T_c 1D$  code.

## 3 Results

205

# 200 3.1 Erosional exhumation-type thermal histories

Twelve EE scenarios were explored, in which various magnitudes of exhumation and internal heat production, and different exhumation histories were applied over the 50 Myr of model run time (Fig. 2c; Table 1).

EE1, in which 10 km of material was removed via constant exhumation at a rate of 0.2 km/Myr, shows FM and MM thermal histories for the final surface particle that are slightly concave upwards, reflecting the modest rate of exhumation. Tracked particles start cooling from  $\approx 290^{\circ}$  C and  $\approx 320^{\circ}$  C for the FM and MM model variants, respectively, reaching  $0^{\circ}$  C at 0 Ma, or



225

235

240



the model present (Fig. 3a). The different initial temperature at 10 km depth for the FM history versus the MM history relates to the differing initial Moho depths (35 km vs. 45 km, respectively), and initial temperatures at the Moho ( $\approx 700^{\circ}$  C and  $\approx 900^{\circ}$  C, respectively; see also supplementary plots under Code and data availability), which together result in different geothermal gradients and crustal temperature evolutions for the two scenarios. Both final surface particle starting temperatures are likely hot enough to produce open system/annealing behavior in all four low-temperature thermochronometers. The thermochronometer closure/annealing temperatures between the FM and MM scenarios are nearly identical, but the ages differ between the two scenarios because of the different thermal histories. The ZFT age for the MM scenario is  $\approx 8$  Myr (or  $\approx 20$  %) younger than for the FM scenario, with smaller differences in cooling age for the lower temperature thermochronometers as the two thermal histories converge towards 0 Ma at the surface.

EE2 is nearly identical to EE1, with 10 km of material being removed via constant exhumation, except the internal heat production of the (entire) crust is lowered to  $1~\mu W \cdot m^{-3}$ . The thermal history for the final surface particle in EE2 is similar to EE1, but with much cooler starting temperatures of  $\approx 200^{\circ}$  C for the FM and MM scenarios, corresponding to an initial geothermal gradient for the upper 10 km of crust of only about  $20^{\circ}$  C/km. These lower initial temperatures are within or cooler than the partial annealing temperature range for ZFT, so the ZFT age is ignored here and in all subsequent models for which total exhumation is only 10 km. The thermal history trajectories for the FM and MM scenarios show less difference than in EE1. This is a result of having less difference in their geotherms at shallow depths due to the lower radiogenic heat production value, despite similarly large contrasts in starting Moho temperature of  $\approx 500^{\circ}$  C and  $\approx 700^{\circ}$  C, respectively. All cooling ages are about 30 % older than in EE1 (e.g., ZHe ages are  $\approx 10$  Myr older, AFT ages are  $\approx 7$  Myr older), largely a result of the cooler initial temperature of the final surface particles.

EE3 and EE4 are two-stage linear exhumation models that incorporate the same total amount of exhumation and internal heat production as in EE2, but either an initial 5 Myr period of rapid exhumation at 1 km/Myr followed by slower exhumation at  $\approx 0.1$  km/Myr over the remaining 45 Myr (EE3), or slower exhumation during the initial 45 Myr and a final 5 Myr period of rapid exhumation (EE4). In EE3, the early, rapid exhumation results in significantly older ages compared to EE2, while in EE4 the late rapid exhumation results in significantly younger low-temperature thermochronometer ages. Note that despite the common erosion rate while traversing the effective closure temperatures of the ZHe and AFT systems for these two models, the lag between the two systems is much shorter for EE3 (< 5 Myr) than for EE4 (> 10 Myr), due to the immediately preceding period of rapid erosion and cooling.

EE5 and EE6 represent fairly extreme erosional models in which 20 km of crust is removed in 50 Myr, corresponding to a long-lived constant erosion rate of 0.4 km/Myr. The difference in Moho depth in the MM scenario thus also differs by 20 km, resulting in an unrealistically hot starting Moho temperature of  $\approx 1200^{\circ}$  C for EE5, in which the crust has a high heat production value (2  $\mu$ W·m<sup>-3</sup>), and  $> 850^{\circ}$  C for EE6, in which the crust has an average heat production value (1  $\mu$ W·m<sup>-3</sup>). Though these are high Moho temperatures, the models are nevertheless instructive in accentuating the heat conduction effects observed in EE1 and EE2.

The cooling paths in EE5 and EE6 show more curvature than in EE1 and EE2, despite the constant erosion rate, as the final surface particle begins closer to the Moho and farther from the surface. The cooling rate initially is low following the onset of





245

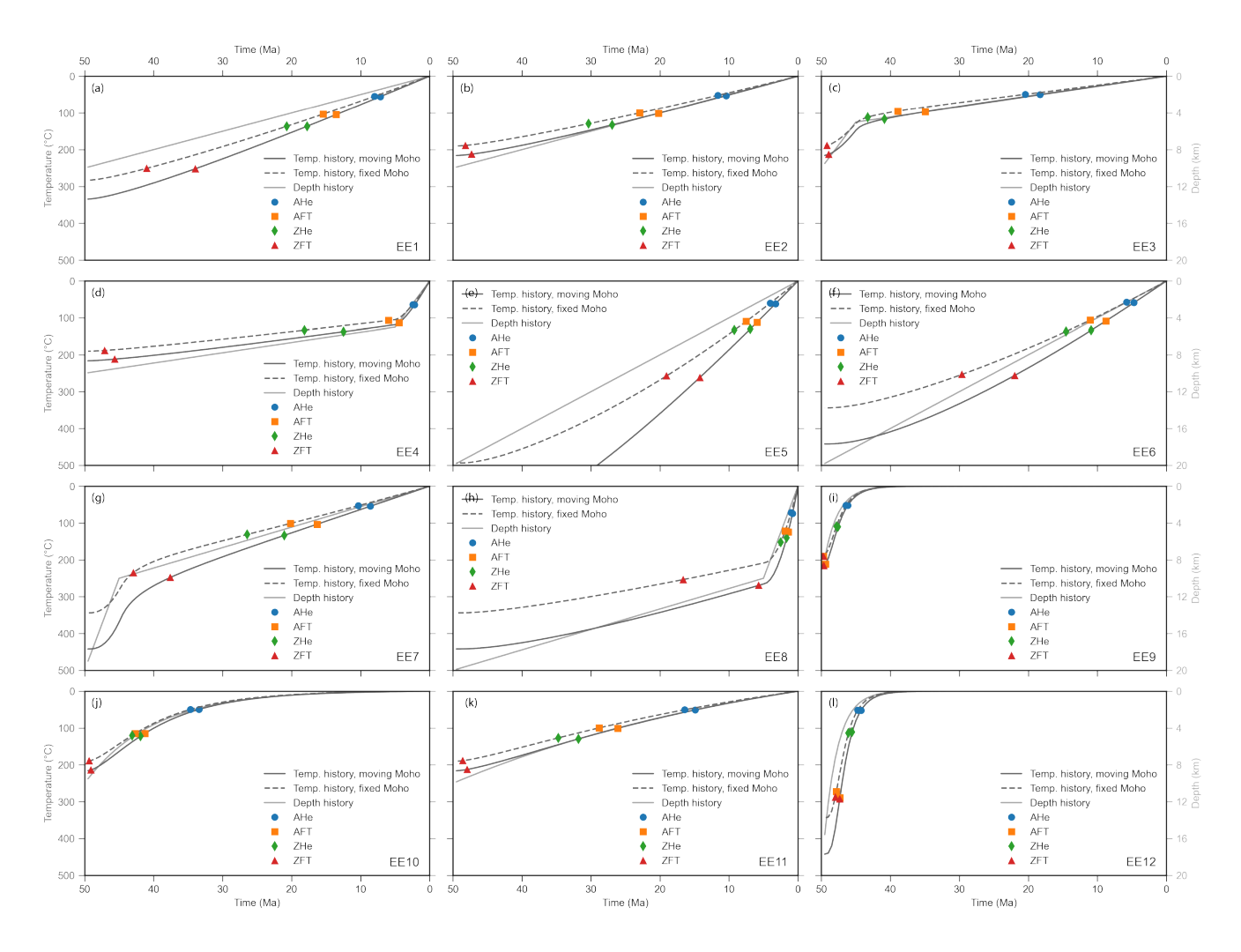


**Figure 3.** Erosional exhumation models. (a)–(l) show results for models EE1–EE12, respectively. Parameters varied in each model are described in Table 1.

exhumation (and heat advection) before beginning to increase and produce a curved cooling trajectory. As the tracking particle nears the surface, the cooling path becomes more linear through the upper  $10~\rm km$  of exhumation, similar to EE1 and EE2. In these and all EE models, the shape of the thermal and depth histories match most closely in the uppermost crust, below  $\sim 10~\rm km$  depth and  $\sim 250^{\circ}$  C and mainly show deviations at higher temperatures and deeper crustal depths. The ages for the four thermochronometers are clustered most closely in EE5, and particularly in the EE5 MM scenario, compared to any of the other scenarios explored thus far, spanning ca.  $10~\rm Myr$ . This reflects the high geothermal gradient from the high, sustained exhumation rate and high heat production for EE5. ZHe and AFT ages are particularly close and would be indistinguishable for typical reported errors of those methods.



250

255

260

265

270

275



Similar to EE3 and EE4, scenarios EE7 and EE8 explore two-stage linear exhumation models, but in which half of the 20 km total exhumation occurs in either the first 5 million years of run time (EE7) or the last 5 million years of run time (EE8) at a rate of 2 km/Myr, and erosion throughout the remainder of each model occurring at  $\approx 0.2$  km/Myr. In both FM and MM versions of EE7, the period of rapid exhumation at the model start shows a significant geometric deviation between the linear depth history and an S-shaped thermal history. The initial period of rapid exhumation advects heat upwards with limited cooling and the thermal adjustment to the slower cooling rate then lags behind the decrease in the exhumation rate. Thus, cooling ages may similarly lag behind the change in exhumation rate. However, since all thermochronometers close on the slow-exhumation segment of the depth history path, this deviation does not impact cooling ages in EE7, and the cooling age patterns in the MM and FM models are relatively similar to EE1. In EE8, there is a similar lag in the thermal history compared to the depth history during the rapid exhumation phase, here occurring in the last 5 Myr of the model, although the deviation is much smaller than in EE7 due to being closer to the model surface, with limited space to exhume without cooling. In this model, the difference in depth history for the FM vs MM scenarios results in a much older ZFT age in the FM scenario, despite its lower calculated effective closure temperature. Otherwise, rapid cooling through the upper crust shows a relatively close alignment between thermal and depth histories, and between the FM and MM scenarios.

In scenarios EE9-EE12, exponentially decaying exhumation rates are explored, with short (EE9), medium (EE10), and long (EE11) characteristic decay times of 2, 10, and 50 Myr, respectively. Each model involves erosional removal of 10 km of crust, as well as an exhumation scenario with 20 km of erosional exhumation (EE12) and a 2 Myr characteristic time. The low decay scenario, EE11, has a gently-curving, near linear cooling path, making it quite similar to EE2. However, the medium and high exponent scenarios (EE9, EE10, EE12) show FM and MM thermal histories that quite closely follow the depth history, in contrast to most of the linear exhumation scenarios described above. In EE10, there is a brief period of limited cooling at the start of the simulation, after which the cooling histories follow the depth history as the exhumation rate decreases. In EE9, the cooling and depth histories are nearly indistinguishable. Although the exhumation rate decays over the same time in EE9 and EE12, the starting depth and rate of exhumation is twice as high in EE12, producing an initial period of limited cooling (where advection dominates conductive cooling) before tracking the shape of the depth history. This initial rapid cooling produces a small lag between the thermal and depth histories. In all of the intermediate and rapidly decaying exponential exhumation rate models (EE9, EE10, and EE12), the thermochronometer ages would be indistinguishable between the FM and MM scenarios within typical reported errors. However, the two high-exponent scenarios (EE9, EE12) both predict an inverted relationship of ZHe ages younger than AFT ages, while the medium exponent scenario in EE10 results in ZHe ages almost equal to AFT ages, matching the pattern reported in Whipp et al. (2022) for low eU-rapid and low eU-intermediate linear cooling rates (see their Fig. 5b).

# 3.2 Sedimentary burial-type thermal histories

Models SB1–SB6 explore the influence of different rates of sedimentary burial and different internal heat production values during burial and exhumation. SB1 and SB2 have intermediate sedimentary burial rates of 0.9 km/Myr for the first 10 Myr followed by 40 Myr of exhumation at a rate of 0.25 km/Myr, and crustal radiogenic heat production values of 2 and 1  $\mu$ W·m<sup>-3</sup>,



285

290

295

300



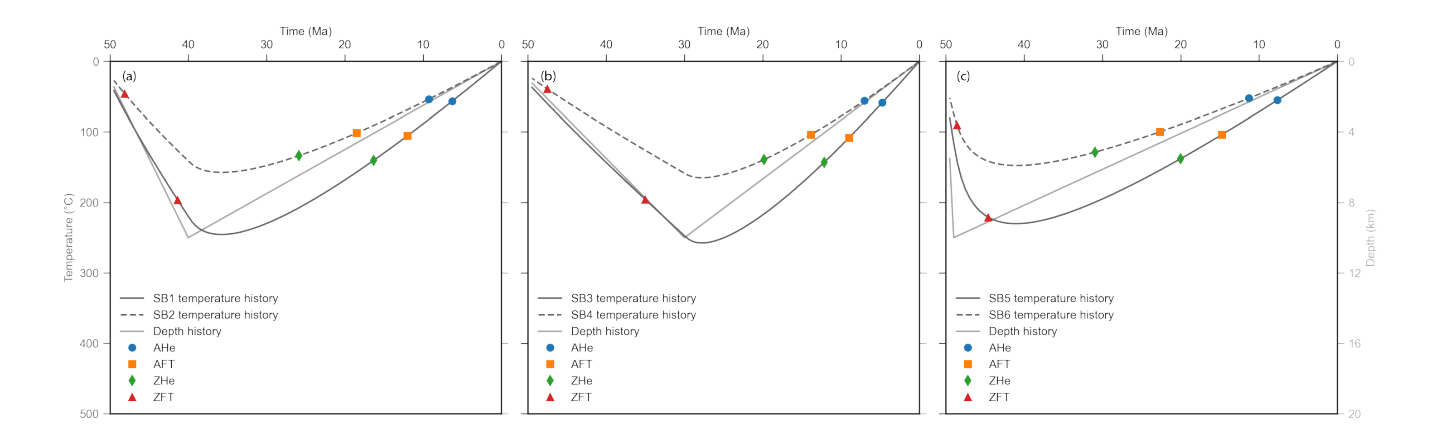


Figure 4. Sedimentary burial models: (a) SB1 and SB2; (b) SB3 and SB4; (c) SB5 and SB6. Parameters varied in each model are described in Table 1.

respectively (Fig. 4a). The peak temperature experienced by the final surface particle in the basement beneath the added sedimentary package reaches  $\approx 240^\circ$  C in SB1 compared to  $\approx 160^\circ$  C in SB2. In both models, the basement rocks reach peak temperatures slightly later than their peak burial depths, lagging by about 4-5 Myr. Cooling ages in the cooler SB2 scenario are significantly older compared to the SB1 scenario (e.g., the ZHe age is almost 10 Myr older) due to the higher peak temperatures associated with higher rates of radiogenic heat production, but the effective closure temperatures are similar. The lag in age between ZHe and AHe is  $\approx 16$  Myr in SB1, compared to  $\approx 10$  Myr in SB2. As with the above EE models, the ZFT thermochronometer does not reach a temperature sufficient for annealing in any of the SB models and is ignored here.

SB3 and SB4 involve the same amount of sedimentary burial and exhumation as SB1 and SB2, except the burial rate is slower (0.45 km/Myr) over 20 Myr and exhumation is more rapid at a rate of  $\approx 0.33$  km/Myr over the remaining 30 Myr (Fig. 4b). As before, SB3 is the high internal heat production scenario, with SB4 being the average (values of 2 and 1  $\mu$ W·m<sup>-3</sup>, respectively). Peak temperatures reached for the final surface particle (corresponding to basement rock originally lying 1 km beneath the eroded basin) in SB3 are  $\approx 250^{\circ}$  C and in SB4 are  $\approx 175^{\circ}$  C, slightly higher than for SB1 and SB2, respectively, due to the slower rate of sedimentation and less cooling from thermal advection. Peak temperature conditions in both scenarios also have a shorter lag following the peak in burial depth, relative to SB1 and SB2, of only 2–3 Myr. This is due to less disturbance of the conductive geotherms from sedimentation at a slower rate. Because of the difference in peak temperature, cooling ages in SB4 are older than in SB3, for example  $\approx 8$  Myr older for the ZHe thermochronometer. The difference in age between ZHe and AHe is  $\approx 12$  Myr in SB3, and  $\approx 8$  Myr in SB4.

The final two scenarios, SB5 and SB6, represent extreme scenarios, with a very high sedimentation rate of 9 km/Myr for 1 Myr followed by slow exhumation at  $\approx 0.2$  km/Myr for the remaining 49 Myr (Fig. 4c). SB5, with high internal heat production (2  $\mu$ W·m<sup>-3</sup>), reaches a peak temperature for the final surface particle of  $\approx 220^{\circ}$  C, while SB6, the average heat production scenario (1  $\mu$ W·m<sup>-3</sup>), reaches a peak temperature of only  $\approx 140^{\circ}$  C, the lowest value among the SB model set. These models also show the longest lag of peak temperature following peak burial depth, at about 8 Myr. Here the rate lag is due to the larger



320

325

330

335



perturbation of the conductive geotherm by the extremely rapid rate of sedimentary burial. Cooling ages in SB6 are > 10 Myr older (ZHe) than in SB5, and the difference in age between ZHe and AHe is  $\approx 20$  Myr in SB5 compared to  $\approx 12$  Myr in SB6.

## 3.3 Thrust faulting-type thermal histories

Models TF1–TF4 explore the effects of thrust faulting on final surface particles in the hanging wall and footwall of a thrust fault (Fig. 5). The fault slip rate (5 km/Myr) and dip angle (30°) are the same in all models, and FM and MM variants are presented. In TF1 and TF2, fault motion is equally partitioned between FW and HW and as explained in Sect. 2.2.3, the initial fault depth b varies for hanging wall and footwall particle, with b = 15.5 km for TF1 and b = 2 km for TF2. In TF1, the HW thermal path for both MM and FM conditions shows a continuous cooling history, with accelerated cooling and exhumation during fault slip, a reduction in cooling immediately after fault motion ends, and a gradual increase in the rate of cooling as the final surface particle is exhumed. The FW thermal histories for this scenario, shown in TF2, show heating during faulting that slightly extends after faulting ceases, delaying significant cooling by around 10 Myr after fault cessation in both FM and MM results. Since the fault position is at a deeper structural level, most of the lower temperature thermochronometers in TF1 and TF2 show similar cooling ages that are strongly influenced by post-faulting exhumation rather than the faulting stage. For instance, the ZHe ages for the MM scenarios in TF1 and TF2 differ only by  $\approx 4$  Myr, which is the largest difference for AHe, AFT, and ZHe. However, the ZFT ages in model TF1 reflect cooling during fault activity, most clearly for the MM scenario. In this case, the ZFT age in the hanging wall is  $\approx 7$  Myr younger than the equivalent age in the footwall, which is unreset.

In scenarios TF3 (HW) and TF4 (FW), the footwall remains fixed with respect to b (Fig. 5c), and all slip is partitioned into hanging wall motion, doubling its rate of motion toward the surface compared to TF1. The thermal history for the HW in this scenario correspondingly shows a more rapid cooling rate during fault slip than for TF1, followed by slower cooling to reach the surface at the end of the model run time than for TF1. As the final surface particle is exhumed closer to the surface during faulting than in TF1, the post-faulting cooling history is more linear compared to the concave upward cooling history in TF1 (Fig. 5a, c). The footwall is held in a fixed position during faulting and then exhumes once faulting has ceased. In this instance, FW heating caused by juxtaposition of the hotter HW is negligible and has no impact on the predicted thermochronometer ages. However, in contrast to TF1, most thermochronometer ages are controlled by fault-related uplift and erosional exhumation, nicely documenting the timing of fault slip in the HW. For example, the AFT, ZHe, and ZFT ages are all  $\approx 45 - 50$  Ma in TF3. In contrast, the AFT, ZHe, and ZFT ages in TF4 are not reset. However, AHe ages are reset in both TF3 and TF4, reflecting post-faulting exhumation and with similar ages ( $\approx 34 - 39$  Ma).

# 3.4 Extensional faulting-type thermal histories

The extensional faulting (EF) models use the same approach as for the TF scenarios, but with a reversed slip direction. Thus, the two different extensional faulting scenarios have a slip rate of 5 km/Myr during 50–45 Ma after an initial 5 Myr of steady state, producing equal end-of-slip fault depths in the upper crust for the HW and FW model variants (8.75 km for EF1 and EF2 and 2.5 km for EF3 and EF4). The final model stage comprises exhumation to the surface at the end of the model (Fig. 5; Table 1). The first set of models (EF1–EF2) use a partitioning factor of 0.5, while for the second set (EF3–EF4) the HW is



340

345



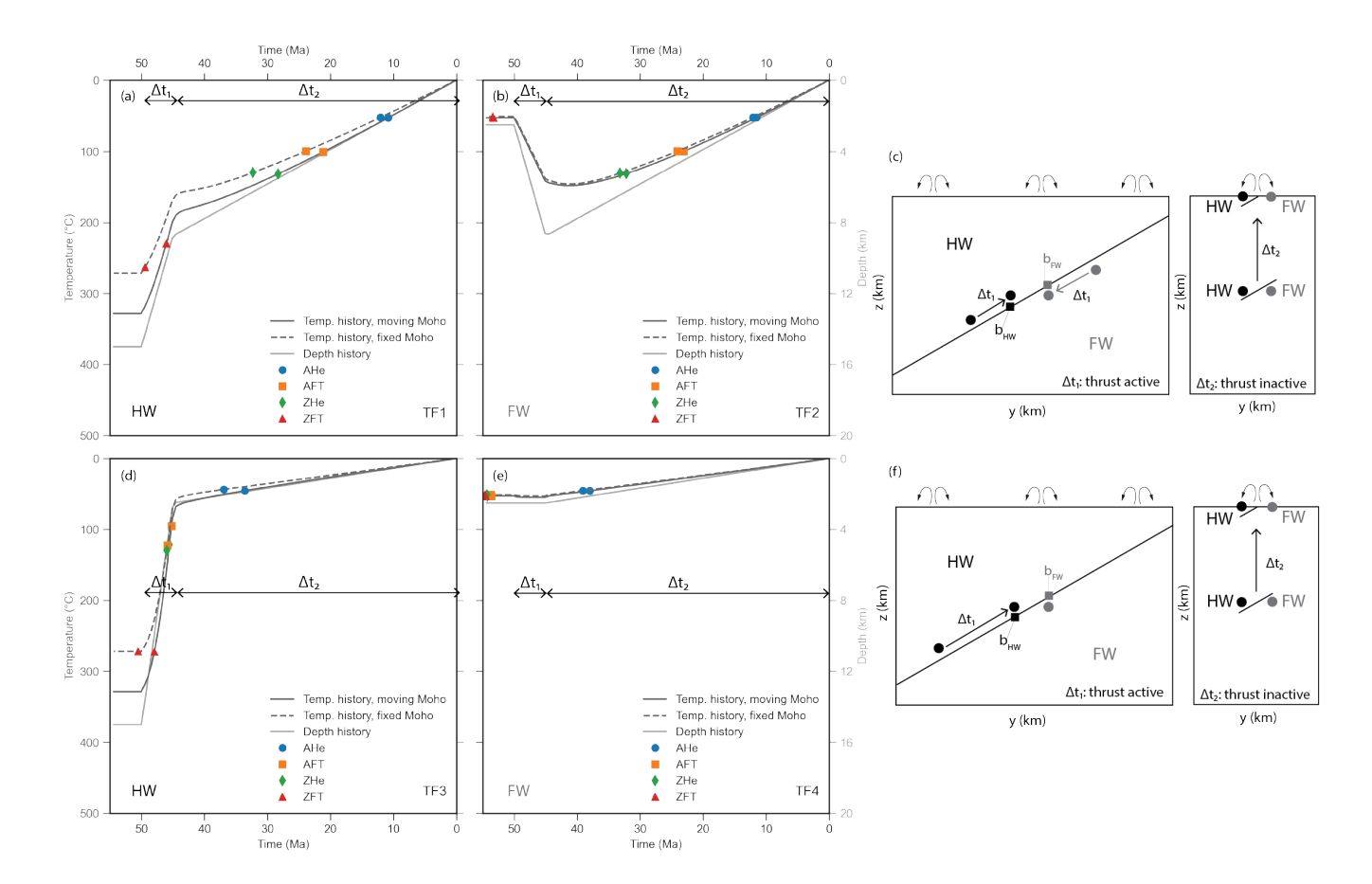


Figure 5. Thrust fault models. (a) and (b) show models TF1 and TF2, which are hanging wall and footwall thermal and depth histories, respectively, simulating the thrust fault displacement scenario described in (c) and Table 1: final surface particle paths for particles that are 500 m above the fault in the hanging wall and 500 m below the fault in the footwall, respectively, of a thrust fault dipping 30°, that was active over 5 Myr during 50–45 Ma with a partitioning factor of  $\lambda = 0.5$  and then exhumed from 8.75 km to the surface. (d) and (e) show models TF3 and TF4, which are hanging wall and footwall thermal and depth histories, respectively, for the fault displacement scenario described in (f) and Table 1: same as TF1 and TF2 but with a fixed footwall ( $\lambda = 0$ ) and exhumation from 2.5 km depth to the surface.

fixed during faulting ( $\lambda = 1$ ). For both scenarios, we examined a final surface particle situated 500 m above the fault in the HW (EF1, EF3), and a final surface particle situated 500 m below the fault in the FW (EF2, EF4).

In EF1 and EF2, the HW is buried from 2.5 km to 8.75 km during fault slip, while the FW block is continuously exhumed from 15 km to 8.75 km during fault slip, and the final surface particle in both scenarios is exhumed at a slower rate to the surface by the end of the model. Here, heating of the HW due to burial and subsequent cooling during exhumation closely follows the depth history of the particle in EF2. This reflects heat from the hot uplifting footwall partially compensating cooling of the HW. Hence, the hanging wall remains closer to conductive thermal equilibrium than it would for a pure burial scenario (e.g., models SB5 and SB6; Fig. 4). In contrast, the greater thickness of uplifting crust in the footwall, compared to the hanging wall, advects



350



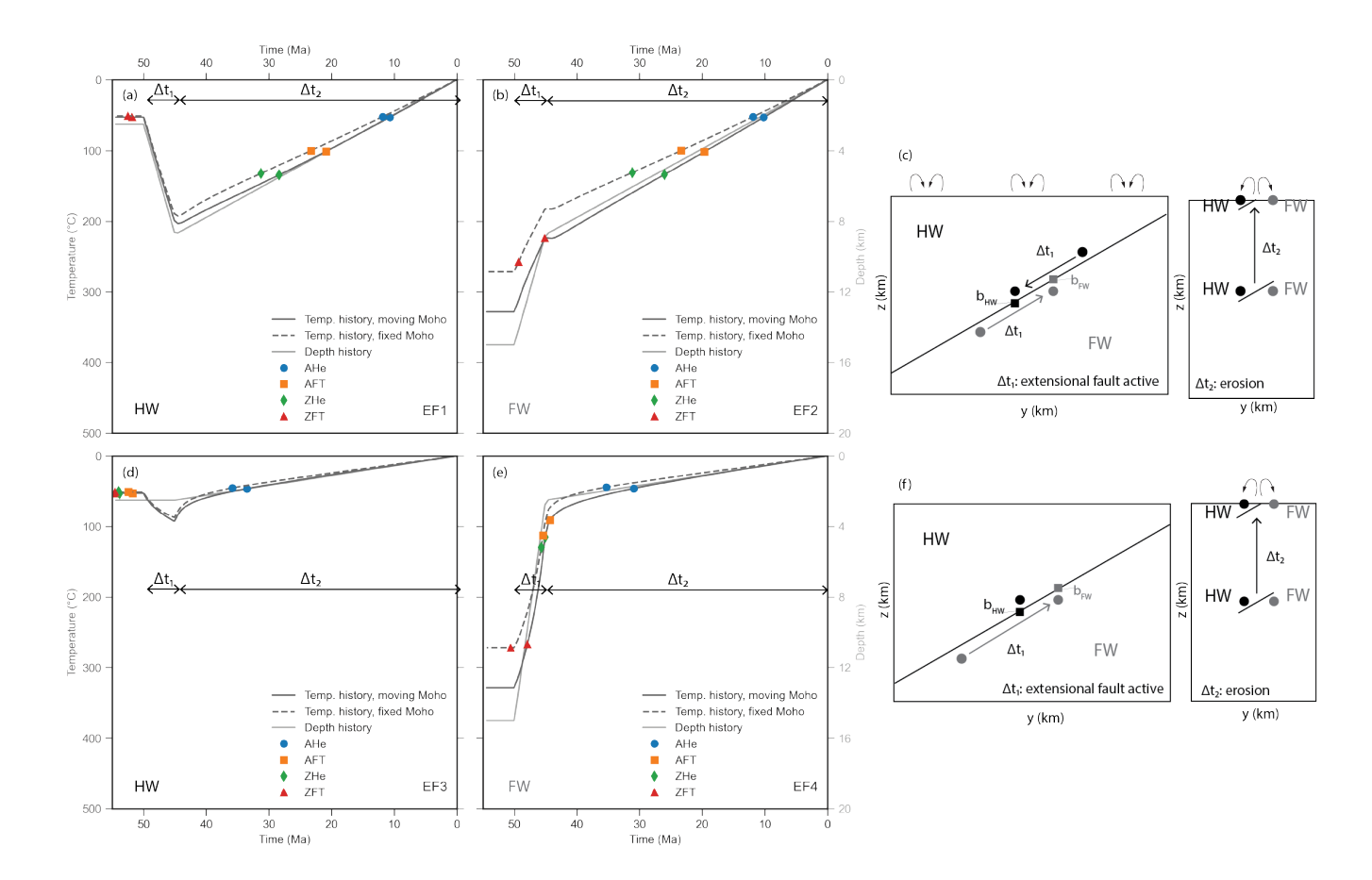


Figure 6. Extensional fault models. (a) and (b) show models EF1 and EF2, respectively, which are hanging wall and footwall thermal and depth histories simulating the fault displacement scenario described in (c) and Table 1: final surface particle paths for particles that are 500 m above the fault in the hanging wall and 500 m below the fault in the footwall, respectively, of an extensional fault dipping 30° that was active over 5 Myr during 50–45 Ma with a partitioning factor of  $\lambda = 0.5$  and then exhumed from 8.75 km to the surface. (d) and (e) show models EF3 and EF4, respectively, which are hanging wall and footwall thermal and depth histories for the fault displacement scenario described in (f) and Table 1: same as EF1 and EF2, but with a fixed hanging wall ( $\lambda = 1$ ), and then exhumed from 2.5 km to the surface.

heat to shallower model depths during faulting, but still produces rapid cooling during fault motion. Faulting-related cooling is then followed by a short pulse of modest heating (1–2 Myr) after fault motion stops. The heating in this case reflects warming of the hanging wall after faulting, due to the onset of exhumation of the entire crust or model thickness. Thermochronometer age patterns in EF1 and EF2 are similar to those observed earlier for TF1 and TF2. The AHe, AFT, and ZHe ages are reset during post-faulting exhumation, the ZFT ages in the exhuming footwall record fault-related cooling, and the ZFT ages in the hanging wall are unreset. Interestingly, the evolution of the Moho depth (fixed vs moving) seems to have more impact on the thermochronometer ages than structural position relative to the fault for TF1 and TF2.



355

360

370

385



In the EF3 and EF4 scenarios, the HW remains fixed during extensional faulting while the FW is exhumed from 15 km to 2.5 km depth (Fig. 6c). Then both the HW and FW are exhumed together to the surface. In this case, heating of the stationary hanging wall in EF3 is clearly visible during and after the period of fault activity in the footwall and followed by slow cooling. The footwall (EF4) shows rapid cooling during faulting, but no period of heating after fault motion stops, as the hanging wall has not cooled like was the case for EF2. Instead, the rate of post-faulting cooling gradually decreases as the final surface particle is exhumed to the surface. Similar to the thrust faulting models TF3 and TF4, only the AHe ages are reset for the hanging wall in EF3, while the rapid cooling during faulting leads to resetting of the AFT, ZHe, and ZFT ages in EF4 (except for ZFT in the FM model variant). As before in TF3, the AHe age in EF4 is reset during post-faulting exhumation.

### 3.5 Lithospheric delamination-type thermal histories

In models DL1–4, delamination is simulated by removal of the underlying lithospheric mantle and juxtaposition of the asthenosphere against the base of the crust at 50 Ma, followed by 15 km of exhumation over the remainder of the model run time (55 Myr). Exhumation styles are similar to scenarios explored in the EE model set, with DL1 involving linear exhumation, and scenarios DL2–4 involving an exponentially decaying rate of erosion with short (2 Myr), medium (10 Myr), and long (50 Myr) exponential decay constants. Each DL model is run with a fixed Moho (FM) and a moving Moho (MM). As for above, the MM scenarios start with a thicker crust (50 km), such that the final Moho depth for FM and MM scenarios is the same, 35 km. For comparison, the individual DL scenarios are plotted against equivalent EE scenarios involving the same magnitude and rate of exhumation, but without lithospheric mantle removal. In this way, it is possible to isolate the influence of bottom-up heating due to the delamination during exhumation of the crust.

Scenario DL1 involves delamination followed by exhumation of 15 km of crust at a constant rate of 0.3 km/Myr (Fig. 7a, b). Cooling ages for both MM (Fig. 7a) and FM (Fig. 7b) are younger than for the EE scenarios without delamination, with cooling not beginning until 5–10 Myr after delamination, despite the continuous rate of exhumation (Fig. 7a). In the MM DL1 scenario, the final surface particle is initially heated by  $\approx 10^{\circ}$  C before beginning its cooling trajectory, resulting in low-temperature thermochronometer ages that are  $\approx 1-5$  million years younger than the corresponding EE scenario. However, in the FM DL1 scenario (Fig. 7b), the final surface particle is heated by  $\approx 100^{\circ}$  C before cooling, and so low-temperature thermochronometer ages are  $\approx 2-18$  Myr younger compared to the EE scenario (e.g., ZFT age  $\approx 28$  Ma in MM DL1 compared to  $\approx 42$  Ma in the corresponding EE scenario). Clearly, delamination leads to conductive heating from the base of the crust and younger ages in both cases, but the thinner initial crustal thickness in the FM model variant shows a larger effect. This general observation of younger ages for DL scenarios relative to the equivalent EE scenario is common to DL1, DL3, and DL4, in both the FM and MM scenarios (Fig. 7).

The DL2 scenarios, with exponential decay of the exhumation rate over a short period (2 Myr), show rapid cooling immediately following delamination (Fig. 7c, d). The final surface particle is transferred quickly into the uppermost crust, escaping delamination-related heating, despite the middle and lower crust experiencing effective temperature increases of up to 250° C in the first 1–5 Myr of model run time, and reaching peak temperatures that are much higher than in DL1 (see supplementary plots link under Code and data availability). The rapid and significant increase in temperature in the middle and lower crust





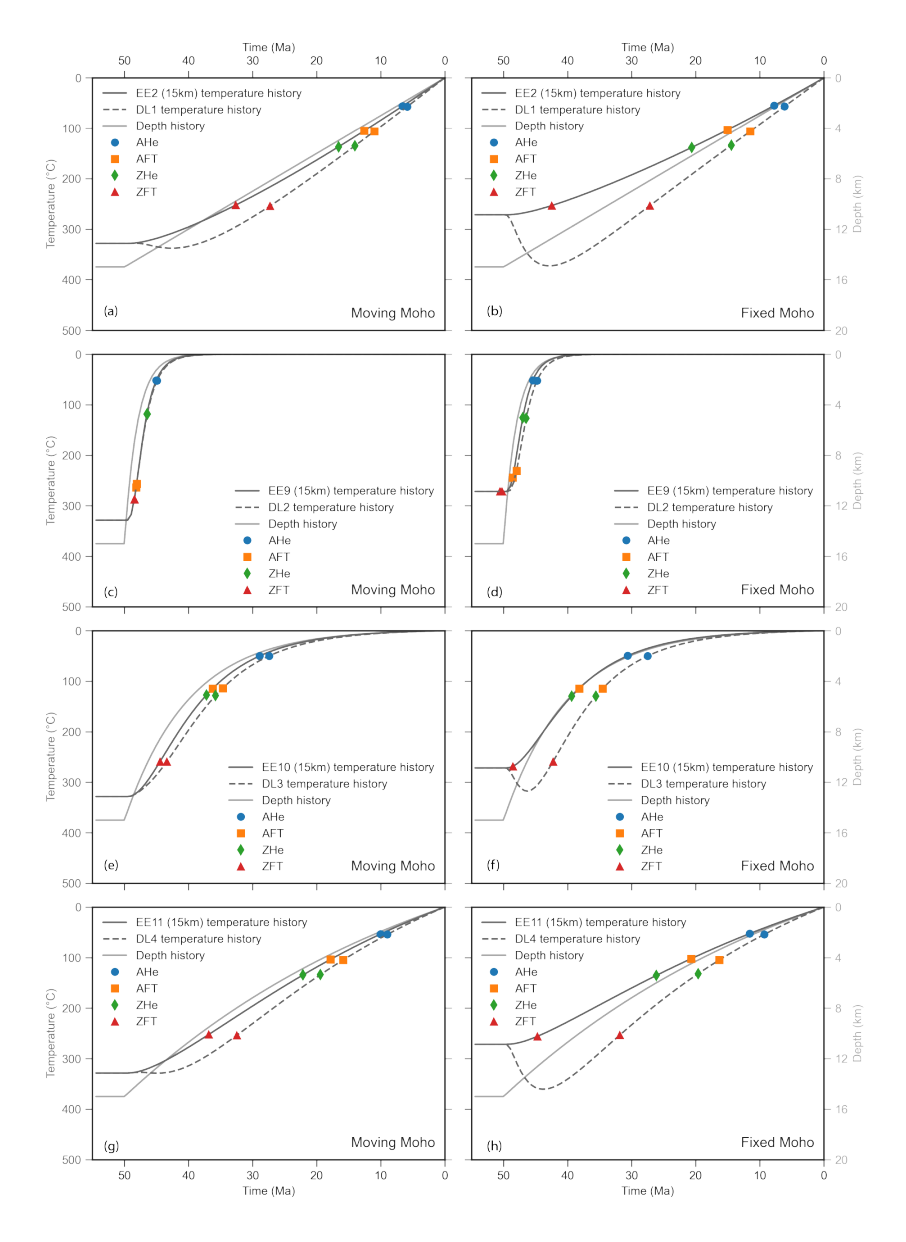


**Figure 7.** Models exploring delamination (DL) of the sub-continental lithosphere coupled with various erosion styles and erosion triggered at the time of delamination. All models start in a steady state at 55 Ma model time and delamination is triggered at 50 Ma model time. For comparison, DL models are plotted together with erosional exhumation (EE) models for the same erosion style so that the thermal effect of delamination can be clearly distinguished. DL1 and EE2 are shown with moving Moho (a) and fixed Moho (b); DL2 and EE9 with moving Moho (c) and fixed Moho (d); DL3 and EE10 with moving Moho (e) and fixed Moho (f), and; DL4 and EE11 with moving Moho (g) and fixed Moho (h). Note that the EE models shown here differ somewhat from those shown in Fig. 3 in that they all involve 15 km of exhumation. See Table 1 for model parameters.



390

415



is a function of both the asthenospheric heating, and the rapid transport of deeper, hotter crust to shallower levels due to the aggressive erosion. As a result, there is almost no difference among the DL2 FM and MM scenarios and their equivalent EE scenarios, despite quite different, rapidly evolving geothermal gradients during the 55 Myr model run time.

The remaining DL scenarios, DL3 and DL4, with erosion occurring via medium and long exponential decay constants, respectively, show thermal histories that are intermediate between DL1 and DL2. Similar to DL1, the FM scenarios (Fig. 7f, h) show between 5–10 Myr of heating before reaching peak temperatures and cooling, representing the interplay of surface processes with a dynamic geothermal gradient over the course of the 55 Myr model run time.

## 4 Discussion

Above we have explored the thermal histories expected to result from a wide range of erosion, sedimentary burial, dip slip faulting, and sub-continental delamination scenarios. In particular, we have demonstrated that each of these geological processes has the potential to decouple a rock's thermal history from its depth history, and that a rock's low temperature thermochronometer ages may show a strong, weak, asynchronous, or no relationship to geological processes that are known to perturb the crustal thermal field, and that are often assumed to be strongly associated in time and space to thermochronometer age data. For example, only some of the fault scenarios explored showed a close relationship between thermochronometer age and the timing of fault slip. Furthermore, the delamination scenarios showed no relationship between thermochronometer age and timing of delamination.

## 4.1 Influence of Moho evolution on low-temperature thermal histories

Since low-temperature thermochronology studies are primarily focused on the evolution of the upper crust, the position and evolution of the Moho during the thermal history under investigation is not typically considered. However, in comparing scenarios in which the Moho depth moves down as material is added at the surface (burial), or shallows as material is removed from the surface (exhumation) with equivalent scenarios in which the Moho depth is held fixed, it is clear that the evolution of the Moho depth can influence upper crustal thermal histories. In most of the model scenarios above (with the exception of the SB scenarios), a FM run was compared against a MM run. FM scenarios are considered to be broadly representative of a syncollisional setting and MM scenarios of a post-tectonic setting (e.g., Wolf et al., 2022), recognizing that this is a simplification and does not address feedback relationships between tectonics and surface processes (Willett, 1999), for example.

The primary observation from these comparisons is that for identical depth histories, the MM or "post-tectonic" models almost always produce younger cooling ages compared to the FM or "collisional" set of models. This pattern of younger MM cooling ages compared to FM cooling ages is consistent among most models run for this study and reflects the higher geothermal gradient in the MM models due to a thicker starting crustal thickness and increased contribution of radiogenic heat production. This produces a higher starting temperature and faster cooling rate during exhumation. In the EE1 case, for example, the starting geothermal gradient of the upper 10 km of crust is only subtly different in the two models at 32° C/km (MM) vs. 29° C/km (FM), yet the resulting ZHe and ZFT ages are 3–7 Myr younger for the MM variant. As would be expected,



420

425

430

440

445

450



the difference in predicted age for FM and MM scenarios decreases when samples are very rapidly exhumed, suggesting the influence of Moho position on thermal histories is less important for such settings.

A notable exception to the trend of younger ages for the MM models is for the models of lithospheric mantle delamination (DL models), where little difference in cooling age is observed for both variants. In the DL models, this is the result of two competing factors that to affect the cooling ages. First, crustal temperatures are higher for scenarios where the crustal thickness is larger, due to a larger contribution of radiogenic heat production over the thicker layer. In contrast, however, heating of the middle and upper crust is greater for delamination models when the crustal thickness is lower, due to heat being conducted across a thinner layer. Thus, heating from delamination is greater at upper crustal levels when the crust is thin, and radiogenic heating of the crust is higher when the crust is thick. For example, the final surface particle in the MM variant of model DL1 starts at a higher temperature than its equivalent in the FM version of DL1 ( $\approx 330^{\circ}$  C versus  $\approx 270^{\circ}$  C; Fig. 7a, b). In many of the other models presented earlier, this would result in younger ages for the MM model. However, the thermal effects of delamination have a larger impact on mid-upper crustal depths in the FM model variant, increasing temperatures by  $\approx 100^{\circ}$  C during exhumation, compared to the more modest temperature increase of  $\approx 10^{\circ}$  C for the MM version of DL1. The result of these competing factors is a set of predicted thermochronometer ages for the FM and MM variants that differ by less than 0.5 Myr.

In general, however, the incorporation of the full lithospheric column into thermal history models has shown that the evolution of the Moho can have a strong influence on the thermal structure of the upper crust and should be given consideration when relating rock thermal histories to geological interpretations.

# 4.2 Relationships between thermal histories and exhumation paths

Although rock cooling in the upper crust can have many causes, it is most commonly considered to be a proxy for rock exhumation (e.g., Reiners et al., 2017), or the approach of a rock towards the Earth's surface. This is because proximity to surface temperatures has a strong control on rock temperature in many, if not most geological settings. The models presented here track both thermal and depth histories of exhumed particles and thus clearly distinguish conditions under which there is a strong relationship between exhumation and thermal history trajectories, and conditions under which they can be decoupled.

Perhaps the most important observation to be made in understanding the relationship between thermal history and exhumation can be observed in comparing models EE1 and EE2. These four scenarios (EE1 (FM), EE1 (MM), EE2 (FM) and EE2 (MM)) share an identical, simple exhumation history and final crustal thickness, but produce four different thermal histories, with cooling ages differing by up to 30 %. This outcome emphasizes the fact that that even a perfectly known thermal history may be derived from multiple non-unique possible geological histories. In these and all EE models, the shape of the thermal and depth history paths match most closely at depths shallower than  $\approx 8$  km and below  $\approx 200^{\circ}$  C and tend to show deviations at high temperatures and deeper crustal depths.

In the models exploring sedimentary burial, the lag time for heating during burial is evident, as is the relative contribution of internal heat production to both heating rate and peak temperature in sedimentary basin settings (Fig. 4). In particular, a





very fast sedimentation/burial rate could manifest in a thermal history as a slower heating event, regardless of heat production values. In contrast, slower sedimentation rates track burial trajectories more closely.

The fault models presented here show the role of heat conduction in cooling hot fault walls and heating cool ones. The examples presented here, however, likely underestimate the heat transfer produced during faulting since frictional heating is ignored.

The effect of lithospheric delamination is to add heat to the crust, which must dissipate to allow low-temperature thermochronometers to reach closure temperature conditions, moving thermochronometer dates farther from the timing of the delamination event than for an identical erosion scenario that lacks a delamination event.

Rapid exhumation scenarios (the exponential decay scenarios with a short decay time: EE12, DL2) are insensitive to bottomup heat advection, or position of the Moho, and show the shortest lag times between individual thermochronometers within a given scenario (i.e., overlapping ZFT, ZHe, AFT, and AHe ages, at typical reported errors), and the narrowest difference in thermochronometer ages between moving Moho and fixed Moho scenarios. We infer from this outcome that closely spaced to overlapping ages from multiple thermochronometers are most likely diagnostic of an aggressive, erosional exhumationdominated system, not a thermal event like delamination or heat transfer by thrust faulting.

## 4.3 Study limitations

470

475

480

485

While we argue that a 1D model can help understand how various geological processes are recorded in thermochronological data, it is important to recognize its inherent limitations, and the limitations of how various geological processes have been implemented. The most obvious limitation is the reduction of 3D geological processes to 1D. Subsurface temperatures in the upper crust are affected by surface topography, which can perturb isotherms to depths of roughly 10 km, depending on the exhumation rate and topographic amplitude and wavelength (e.g., Stüwe et al., 1994). This effect is largest in mountainous regions, and although this process can be accounted for to some degree in 1D models by applying a topographic correction (e.g., Ketcham, 2025), such a correction was not applied here and thus care should be used in comparing our results to data from mountainous regions, as topographic effects are not included. In addition, dip-slip fault motion frequently involves both vertical and horizontal motions, resulting in 2D or 3D thermal advection that perturbs the crustal thermal field in a horizontal direction. This effect would be most significant in the results of Sect. 3.3 and 3.4, where the vertical thermal components of dipslip faulting are simulated for thrust and extensional faults. While the vertical component of motion may be most important for thermochronometer data in rapidly eroding settings (e.g., Whipp et al., 2007), horizontal heat transfer may be more important in regions of active faulting with lower rates of exhumation. Considering both points above, T<sub>c</sub>1D would ideally be applied to interpret data from regions with limited topographic relief, moderate to slow rates of exhumation, and little to no active faulting. In other cases, T<sub>c</sub>1D may be able to provide estimates of data sensitivity to various geological processes, but a detailed analysis of thermochronometer data may require more sophisticated software such as Pecube (Braun, 2003; Braun et al., 2012).

Our results also do not simulate dynamic erosional responses to geological processes, such as increased erosional exhumation following topographic uplift resulting from lithospheric delamination (Sect. 3.5). It is estimated that removal of the mantle lithosphere would trigger isostatic uplift of the surface by  $\sim 1$  km due to the combination of thermal and density changes. This



495

500

505



uplift would likely result a period of increased erosional exhumation that could be simulated with a surface process model, for example. However, surface process models generally require at least two dimensions to simulate hillslope diffusion, and fluvial and glacial erosion processes. It may be possible to link estimated magnitudes of isostatic uplift to a surface process model using  $T_c 1D$  predictions, but this was not done for the presented results. Additionally, such an exercise would require consideration of topographic effects, as mentioned in the previous paragraph.

The effects of melting and magmatic processes are also not included in the  $T_c1D$  results. Partial crustal melting from delamination or magmatic intrusions would be expected to transfer mass, advect heat in the crust, and consume and release

heat during melting and crystallization (e.g., Kay and Mahlburg Kay, 1993). This could be locally important in some settings and in some of the model results presented here, such as those for the delamination models or select erosional exhumation scenarios (Sect. 3.1 and 3.5). For instance, present-day reported Moho temperatures greater than 800° C have been correlated with < 10 Ma magmatism in the overlying crust (e.g., Schutt et al., 2018), and temperatures 850–1000° C in the lower crust are expected to cross the wet granite and dry granite solidi (Stern et al., 1975). Since T<sub>c</sub>1D does not simulate melting and melt transport, the EE5 MM scenario deviates from geological reality. In cases where crustal melting is a concern, it is possible to plot crustal solidi for various rock compositions in T<sub>c</sub>1D to estimate the magnitude of the effects of melting and crystallization. Finally, we note a few additional limitations that may affect the model predictions for different scenarios. The fixed Moho models are presented as analogs to tectonic scenarios where crustal thickening is balanced by erosion in a syn-tectonic erosional scenario. While this is a reasonable approximation for situations where uplift and erosion are close to in balance, this may not apply for early stages of orogenesis where crustal surface uplift may outpace erosion and thicken the crust (e.g., Beaumont et al., 2000). Additionally, sediment compaction is not modeled for the sedimentary burial and erosional exhumation models (Sect. 3.2). In essence, this means that deposited sediments do not compact, though most sediments can compact by more than 40%, depending on composition (e.g., Athy, 1930). The result is that deposited sediment thicknesses are likely overestimated for the erosional exhumation that follows deposition in the T<sub>c</sub>1D models. And finally, the concentration of heat-producing elements in the T<sub>c</sub>1D models presented here is constant with depth, rather than decaying. The option for exponential decay of

## 5 Conclusions

crustal temperatures may be higher than expected for some scenarios.

In conclusion, modeling of the dynamic thermal state of the full lithosphere in 1D allows for testing of expected thermochronometer patterns for a wide range of geological scenarios and parameters. In this contribution, we have modeled a range of erosion, sedimentary burial, fault, and lithospheric delamination scenarios to explore the relationships between those geological processes, the thermal evolution of the lithosphere, and low-temperature thermochronometer ages.

the concentration of heat-producing elements is available in  $T_c 1D$ , but was not used for the presented results. As a result, lower

Low-temperature thermochronology studies primarily focus on the evolution of the upper crust, so the position and evolution of the Moho is not typically considered. Here we demonstrated, however, that the evolution of the Moho depth can influence upper crustal thermal histories. For identical depth histories, Moving Moho ("post-tectonic"-type) models almost always produce

https://doi.org/10.5194/egusphere-2025-5403 Preprint. Discussion started: 12 November 2025

© Author(s) 2025. CC BY 4.0 License.



525

younger cooling ages compared to Fixed Moho ("syn-collisional"-type) models. This is a reflection of the higher geothermal 520 gradient in the Moving Moho models due to a thicker starting crustal thickness and increased contribution of crustal radiogenic heat production.

Several of the modeled scenarios show a strong relationship between exhumation (depth history) and thermal history trajectories. However, our results have identified several scenarios under which depth and thermal histories can be decoupled, such as during rapid burial of radiogenic sediments, in certain faulting scenarios, and during delamination of the lithospheric mantle. Combined, these results suggest that care should be taken when interepreting low-temperature thermochronometer data, and simple models such as  $T_c 1D$  may be useful tools to explore data sensitivity to geological processes.

Code and data availability. Results produced here used the Tc1D software available on GitHub at https://github.com/HUGG/Tc1D. Model output logs and supplementary plots can be found at https://ida.fairdata.fi/s/NOT-FOR-PUBLICATION-ooR8cPJJSHYH.

## **Appendix A: Thrust and extensional fault kinematics**

The kinematics for the thrust faulting (TF) and extensional faulting (EF) models require simulating a 2D (or 3D) process in only 1D. This is done in T<sub>c</sub>1D by removing the horizontal component of the fault velocity field and tracking particle depth relative to the reference frame of the hanging wall or footwall, depending upon where the tracking particle is located (Fig. A1. For a thrust faulting scenario, this reference frame will produce a vertical velocity that moves a tracking particle in the hanging wall upwards at the same velocity as the fault beneath it, maintaining a constant distance above the fault until the particle reaches the surface. This vertical velocity is simply the vertical component of the fault slip velocity. Similarly, a footwall particle will move downwards at the same velocity as the vertical component of fault slip as will the fault above it. Thus, tracking particles will experience different vertical motions, but always maintain a constant vertical distance from the fault during fault motion. Examples of the vertical velocities tracking particles would experience are shown for the TF and EF models in Fig. A1.

Author contributions. Kellett: Conceptualization, formal analysis, investigation, methodology, validation, visualization, writing (original 540 draft preparation), writing (review and editing). Whipp: Conceptualization, data curation, formal analysis, investigation, methodology, software, validation, visualization, writing (original draft preparation), writing (review and editing)

Competing interests. The authors declare that they have no conflict of interest.

Acknowledgements. Kellett acknowledges funding by Natural Resources Canada's Geomapping for Energy and Minerals-GeoNorth program. This contribution benefited from meaningful discussions with Isabelle Coutand, Scott Jess, Sean Kelly, Karl Lang, and Kelly Thomson.





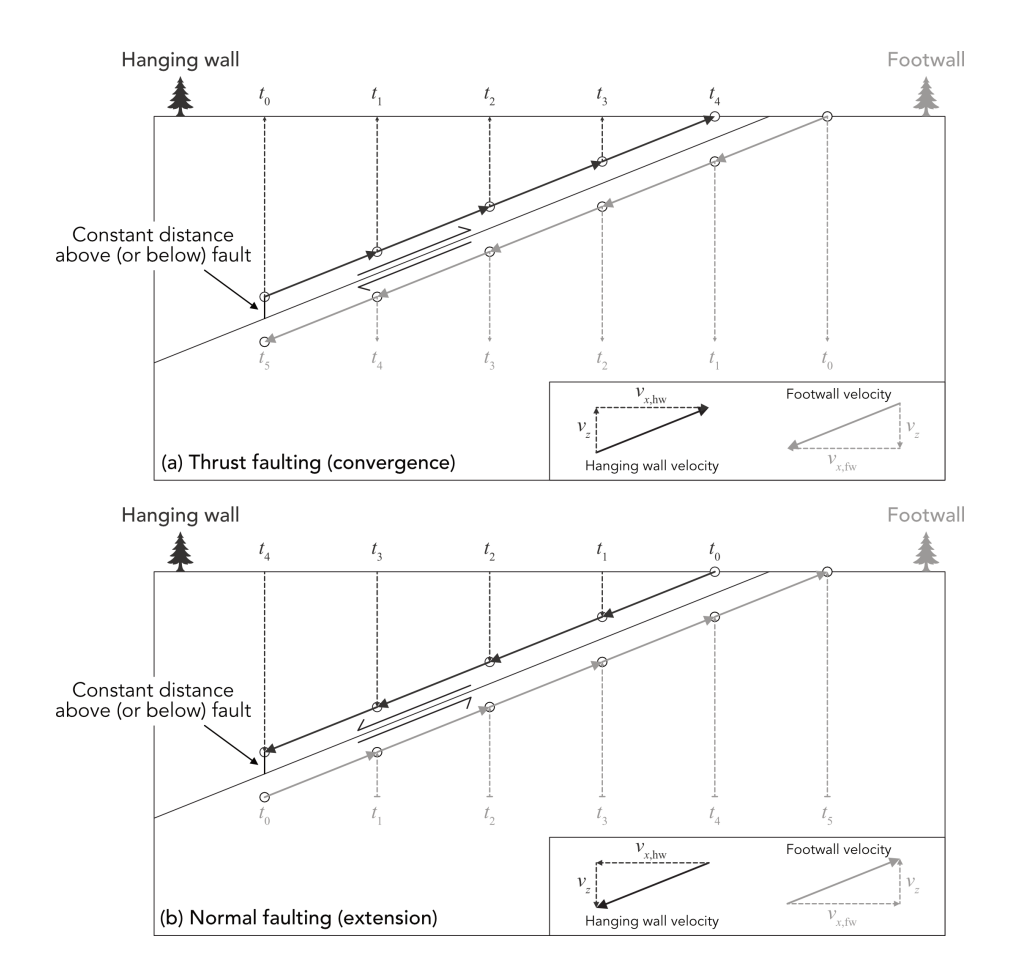


Figure A1. Kinematics of thrust and normal faulting in a reference frame where the fault location is fixed. (a) To an observer standing on the hanging wall of a thrust fault, the fault and tracking particle get shallower with time during fault motion. Thus, to them  $v_{x,\text{hw}}=0$ . Conversely, to an observer standing on the footwall, the fault and particle get deeper and  $v_{x,\text{fw}}=0$  in their reference frame. (b) To an observer standing on the hanging wall of a normal fault, the fault and tracking particle get deeper with time during fault motion and again  $v_{x,\text{hw}}=0$  to them. In contrast, the fault and particle get shallower to an observer standing on the footwall, and in their reference frame  $v_{x,\text{fw}}=0$  again. In all cases,  $v_x$  is the horizontal velocity,  $v_z$  is the vertical velocity, and time increases from  $t_0$  to  $t_5$ .

## 545 References

Athy, L. F.: Density, Porosity, and Compaction of Sedimentary Rocks, AAPG Bulletin, 14, 1–24, https://doi.org/10.1306/3D93289E-16B1-11D7-8645000102C1865D, 1930.

Bao, X., Eaton, D. W., and Guest, B.: Plateau Uplift in Western Canada Caused by Lithospheric Delamination along a Craton Edge, Nature Geoscience, 7, 830–833, https://doi.org/10.1038/ngeo2270, 2014.



555

565

570



- Beaumont, C., Kooi, H., and Willett, S. D.: Coupled Tectonic-Surface Process Models with Applications to Rifted Margins and Collisional Orogens, in: Geomorphology and Global Tectonics, edited by Summerfield, M. A., p. 367, John Wiley & Sons, Ltd., West Sussex, U.K., 2000.
  - Bezada, M. J., Humphreys, E. D., Davila, J., Carbonell, R., Harnafi, M., Palomeras, I., and Levander, A.: Piecewise Delamination of Moroccan Lithosphere from beneath the Atlas Mountains, Geochemistry, Geophysics, Geosystems, 15, 975–985, https://doi.org/10.1002/2013GC005059, 2014.
  - Bidgoli, T. S., Amir, E., Walker, J. D., Stockli, D. F., Andrew, J. E., and Caskey, S. J.: Low-Temperature Thermochronology of the Black and Panamint Mountains, Death Valley, California: Implications for Geodynamic Controls on Cenozoic Intraplate Strain, Lithosphere, https://doi.org/10.1130/L406.1, 2015.
- Braun, J.: Pecube: A New Finite-Element Code to Solve the 3D Heat Transport Equation Including the Effects of a Time-Varying, Finite

  Amplitude Surface Topography, Computers & Geosciences, 29, 787–794, 2003.
  - Braun, J., van der Beek, P., Valla, P. G., Robert, X., Herman, F., Glotzbach, C., Pedersen, V., Perry, C., Simon-Labric, T., and Prigent, C.: Quantifying Rates of Landscape Evolution and Tectonic Processes by Thermochronology and Numerical Modeling of Crustal Heat Transport Using PECUBE, Tectonophysics, 524\text{textendash525}, 1–28, 2012.
  - Dai, J., Wang, C., Hourigan, J., Li, Z., and Zhuang, G.: Exhumation History of the Gangdese Batholith, Southern Tibetan Plateau: Evidence from Apatite and Zircon (U-Th)/He Thermochronology, The Journal of Geology, 121, 155–172, https://doi.org/10.1086/669250, 2013.
  - Drew, S. T., Ducea, M. N., and Schoenbohm, L. M.: Mafic Volcanism on the Puna Plateau, NW Argentina: Implications for Lithospheric Composition and Evolution with an Emphasis on Lithospheric Foundering, Lithosphere, 1, 305–318, https://doi.org/10.1130/L54.1, 2009. Ducea, M. N.: Fingerprinting Orogenic Delamination, Geology, 39, 191–192, https://doi.org/10.1130/focus022011.1, 2011.
  - Ehlers, T. A.: Crustal Thermal Processes and the Interpretation of Thermochronometer Data, in: Low-Temperature Thermochronology: Techniques, Interpretations and Applications, pp. 315–350, Mineralogical Society of America, 2005.
  - Flowers, R. M., Ketcham, R. A., Shuster, D. L., and Farley, K. A.: Apatite (U-Th)/He Thermochronometry Using a Radiation Damage Accumulation and Annealing Model, Geochimica et Cosmochimica Acta, 73, 2347–2365, 2009.
    - Flowers, R. M., Farley, K. A., and Ketcham, R. A.: A Reporting Protocol for Thermochronologic Modeling Illustrated with Data from the Grand Canyon, Earth and Planetary Science Letters, 432, 425–435, https://doi.org/10.1016/j.epsl.2015.09.053, 2015.
- Fraser, K. I., Enkelmann, E., Jess, S., Gilbert, H., and Grieco, R.: Resolving the Cenozoic History of Rock Exhumation Along the Central Rocky Mountain Trench Using Apatite Low-Temperature Thermochronology, Tectonics, 40, e2021TC006847, https://doi.org/10.1029/2021TC006847, 2021.
  - Gallagher, K.: Transdimensional Inverse Thermal History Modeling for Quantitative Thermochronology, Journal of Geophysical Research: Solid Earth, 117, https://doi.org/10.1029/2011JB008825, 2012.
- Garzione, C. N., Molnar, P., Libarkin, J. C., and MacFadden, B. J.: Rapid Late Miocene Rise of the Bolivian Altiplano: Evidence for Removal of Mantle Lithosphere, Earth and Planetary Science Letters, 241, 543–556, https://doi.org/http://dx.doi.org/10.1016/j.epsl.2005.11.026, 2006.
  - Garzione, C. N., Hoke, G. D., Libarkin, J. C., Withers, S., MacFadden, B., Eiler, J., Ghosh, P., and Mulch, A.: Rise of the Andes, Science, 320, 1304–1307, 2008.
- 585 Göğüş, O. H. and Ueda, K.: Peeling Back the Lithosphere: Controlling Parameters, Surface Expressions and the Future Directions in Delamination Modeling, Journal of Geodynamics, 117, 21–40, https://doi.org/10.1016/j.jog.2018.03.003, 2018.



600



- Guenthner, W. R.: Implementation of an Alpha Damage Annealing Model for Zircon (U-Th)/He Thermochronology With Comparison to a Zircon Fission Track Annealing Model, Geochemistry, Geophysics, Geosystems, 22, e2019GC008757, https://doi.org/10.1029/2019GC008757, 2021.
- Guenthner, W. R., Reiners, P. W., Ketcham, R. A., Nasdala, L., and Giester, G.: Helium Diffusion in Natural Zircon: Radiation Damage, Anisotropy, and the Interpretation of Zircon (U-Th)/He Thermochronology, American Journal of Science, 313, 145–198, https://doi.org/10.2475/03.2013.01, 2013.
  - Kay, R. W. and Mahlburg Kay, S.: Delamination and Delamination Magmatism, Tectonophysics, 219, 177–189, https://doi.org/10.1016/0040-1951(93)90295-U, 1993.
- Ketcham, R. A.: Forward and Inverse Modeling of Low-Temperature Thermochronometry Data, in: Low-Temperature Thermochronology: Techniques, Interpretations and Applications, pp. 275–314, Mineralogical Society of America, 2005.
  - Ketcham, R. A.: Technical Note: Incorporating Topographic Deflection Effects into Thermal History Modelling, EGUsphere, pp. 1–14, https://doi.org/10.5194/egusphere-2025-901, 2025.
  - Ketcham, R. A., Donelick, R. A., and Carlson, W. D.: Variability of Apatite Fission-Track Annealing Kinetics; III, Extrapolation to Geological Time Scales, American Mineralogist, 84, 1235–1255, 1999.
  - Ketcham, R. A., Donelick, R. A., and Donelick, M. B.: AFTSolve: A Program for Multi-Kinetic Modeling of Apatite Fission-Track Data, Geological Materials Research, 2, 1–32, 2000.
  - Ketcham, R. A., Mora, A., and Parra, M.: Deciphering Exhumation and Burial History with Multi-Sample down-Well Thermochronometric Inverse Modelling, Basin Research, 30, 48–64, https://doi.org/10.1111/bre.12207, 2018.
- 605 Lock, J. and Willett, S.: Low-Temperature Thermochronometric Ages in Fold-and-Thrust Belts, Tectonophysics, 456, 147–162, 2008.
  - Mansour, J., Giordani, J., Moresi, L., Beucher, R., Kaluza, O., Velic, M., Farrington, R., Quenette, S., and Beall, A.: Underworld2: Python Geodynamics Modelling for Desktop, HPC and Cloud, Journal of Open Source Software, 5, 1797, https://doi.org/10.21105/joss.01797, 2020.
- McMillan, M. and Schoenbohm, L. M.: Diverse Styles of Lithospheric Dripping: Synthesizing Gravitational Instability

  Models, Continental Tectonics, and Geologic Observations, Geochemistry, Geophysics, Geosystems, 24, e2022GC010488, https://doi.org/10.1029/2022GC010488, 2023.
  - McQuarrie, N. and Ehlers, T. A.: Influence of Thrust Belt Geometry and Shortening Rate on Thermochronometer Cooling Ages: Insights from Thermokinematic and Erosion Modeling of the Bhutan Himalaya, Tectonics, 34, 1055–1079, 2015.
- McQuarrie, N., Ehlers, T. A., Law, R. D., Thigpen, J. R., Merschat, A. J., and Stowell, H. H.: Techniques for Understanding Fold-and-Thrust Belt Kinematics and Thermal Evolution, in: Linkages and Feedbacks in Orogenic Systems, Geological Society of America, ISBN 978-0-8137-1213-0, 2017.
  - Oxburgh, E. R. and Turcotte, D. L.: Thermal Gradients and Regional Metamorphism in Overthrust Terrains with Special Reference to the Eastern Alps, Schweizerische mineralogische und petrographische Mitteilungen, 54, https://doi.org/10.5169/seals-42213, 1974.
- Rahn, M. K., Brandon, M. T., Batt, G. E., and Garver, J. I.: A Zero-Damage Model for Fission-Track Annealing in Zircon, American Mineralogist, 89, 473–484, https://doi.org/10.2138/am-2004-0401, 2004.
  - Reiners, P. W., Carlson, R. W., Renne, P. R., Cooper, K. M., Granger, D. E., McLean, N. M., and Schoene, B.: Geochronology and Thermochronology, John Wiley & Sons, 2017.
  - Salles, T. and Hardiman, L.: Badlands: An Open-Source, Flexible and Parallel Framework to Study Landscape Dynamics, Computers & Geosciences, 91, 77–89, https://doi.org/10.1016/j.cageo.2016.03.011, 2016.





- 625 Schutt, D. L., Lowry, A. R., and Buehler, J. S.: Moho Temperature and Mobility of Lower Crust in the Western United States, Geology, 46, 219–222, https://doi.org/10.1130/G39507.1, 2018.
  - Stern, C. R., Huang, W.-L., and Wyllie, P. J.: Basalt-Andesite-Rhyolite-H2O: Crystallization Intervals with Excess H2O and H2O-undersaturated Liquidus Surfaces to 35 Kilobars, with Implications for Magma Genesis, Earth and Planetary Science Letters, 28, 189–196, https://doi.org/10.1016/0012-821X(75)90226-5, 1975.
- Stockli, D. F.: Application of Low-Temperature Thermochronometry to Extensional Tectonic Settings, in: Low-Temperature Thermochronology: Techniques, Interpretations and Applications, pp. 411–448, Mineralogical Society of America, 2005.
  - Stüwe, K., White, L., and Brown, R.: The Influence of Eroding Topography on Steady-State Isotherms; Application to Fission Track Analysis, Earth and Planetary Science Letters, 124, 63–74, 1994.
- Tagami, T., Galbraith, R. F., Yamada, R., and Laslett, G. M.: Revised Annealing Kinetics of Fission Tracks in Zircon and Geological Implications, in: Advances in Fission-Track Geochronology: A Selection of Papers Presented at the International Workshop on Fission-Track Dating, Ghent, Belgium, 1996, edited by van den Haute, P. and de Corte, F., pp. 99–112, Springer Netherlands, Dordrecht, ISBN 978-94-015-9133-1, https://doi.org/10.1007/978-94-015-9133-1 8, 1998.
  - Turcotte, D. L. and Schubert, G.: Geodynamics, Cambridge University Press, Cambridge, UK, 3rd edn., 2014.
- van der Beek, P., Andriessen, P., and Cloetingh, S.: Morphotectonic Evolution of Rifted Continental Margins: Inferences from a Coupled

  Tectonic-Surface Processes Model and Fission Track Thermochronology, Tectonics, 14, 406–421, https://doi.org/10.1029/94TC02445,
  1995.
  - Whipp, D. M.: Tc1D: A 1D Thermal and Thermochronometer Age Prediction Model, https://doi.org/10.5281/zenodo.7124271, 2022.
  - Whipp, D. M., Ehlers, T. A., Blythe, A. E., Huntington, K. W., Hodges, K. V., and Burbank, D. W.: Plio-Quaternary Exhumation History of the Central Nepalese Himalaya: 2. Thermo-kinematic and Thermochronometer Age Prediction Model, Tectonics, 26, 2007.
- Whipp, D. M., Kellett, D. A., Coutand, I., and Ketcham, R. A.: Short Communication: Modeling Competing Effects of Cooling Rate, Grain Size, and Radiation Damage in Low-Temperature Thermochronometers, Geochronology, 4, 143–152, https://doi.org/10.5194/gchron-4-143-2022, 2022.
  - Willett, S. D.: Orogeny and Orography; the Effects of Erosion on the Structure of Mountain Belts, Journal of Geophysical Research, B, Solid Earth and Planets, 104, 28,957–28,982, 1999.
- Wolf, S. G., Huismans, R. S., Braun, J., and Yuan, X.: Topography of Mountain Belts Controlled by Rheology and Surface Processes, Nature, pp. 1–6, https://doi.org/10.1038/s41586-022-04700-6, 2022.
  - Zandt, G., Gilbert, H., Owens, T. J., Ducea, M., Saleeby, J., and Jones, C. H.: Active Foundering of a Continental Arc Root beneath the Southern Sierra Nevada in California, Nature, 431, 41–46, https://doi.org/10.1038/nature02847, 2004.